Regular Article

Porous micropillar structures for retaining low surface tension liquids

Damena D. Agonafer [a,1,*], Hyoungsoon Lee [b,1], Pablo A. Vasquez [c], Yoonjin Won [d], Ki Wook Jung [c], Srilakshmi Lingamneni [c], Binjian Ma [a], Li Shan [a], Shuai Shuai [a], Zichen Du [a], Tanmoy Maitra [c], James W. Palko [e], Kenneth E. Goodson [c]

[a] Department of Mechanical Engineering & Materials Science, Washington University in Saint Louis, Saint Louis, MO, 63130-4899, USA
[b] School of Mechanical Engineering, Chung-Ang University, Seoul 06974, South Korea
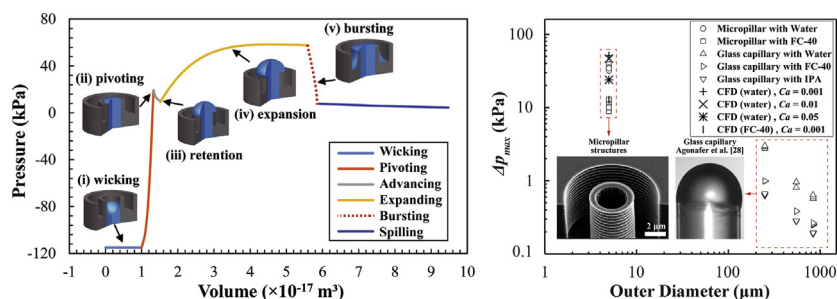[c] Department of Mechanical Engineering, Stanford University, Stanford, CA, 94305-3030, USA
[d] Department of Mechanical and Aerospace Engineering, University of California at Irvine, Irvine, CA 92697, USA
[e] Department of Mechanical Engineering, University of California, Merced, CA 95340, USA

G R A P H I C A L   A B S T R A C T

A R T I C L E   I N F O

A B S T R A C T

The ability to manipulate fluid interfaces, e.g., to retain liquid behind or within porous structures, can be beneficial in multiple applications, including microfluidics, biochemical analysis, and the thermal management of electronic systems. While there are a variety of strategies for controlling the disposition of liquid water via capillarity, such as the use of chemically modified porous adhesive structures and capillary stop valves or surface geometric features, methods that work well for low surface tension liquids are far more difficult to implement. This study demonstrates the microfabrication of a silicon membrane that can retain exceptionally low surface tension fluorinated liquids against a significant pressure difference across the membrane via an array of porous micropillar structures. The membrane uses capillary forces along the triple phase contact line to maintain stable liquid menisci that yield positive working Laplace pressures. The micropillars have inner diameters and thicknesses of 1.5–3 μm and ∼1 μm, respectively, sustaining Laplace pressures up to 39 kPa for water and 9 kPa for Fluorinert™ (FC-40). A theoretical model for predicting the change in pressure as the liquid advances along the porous micropillar structure is derived based on a free energy analysis of the liquid meniscus with capped spherical geometry. The theoretical prediction was found to overestimate the burst pressure compared with the experimental measurements. To elucidate this deviation, transient numerical simulations based on the Volume of Fluid (VOF) were performed to explore the liquid pressure and evolution of meniscus shape under different flow rates (i.e., Capillary numbers). The results from VOF simulations reveal strong dynamic effects where the anisotropic expansion of liquid along the outer micropillar edge leads to an irregular meniscus shape before the liquid spills along the micropillar edge. These findings suggest that the analytical

* Corresponding author.
E-mail address: agonafer@wustl.edu (D.D. Agonafer).
[1] These authors contributed equally to this work.

Nomenclature

Bo	bond number ($\rho g L^2/\gamma$)
CAH	contact angle hysteresis
Ca	capillary number ($\mu V/\gamma$)
D	micropillar outer diameter (m)
D_t	trench diameter (m)
d	micropillar inner diameter (m)
E	free energy (J)
F	force (N)
g	gravitational acceleration (m/s^2)
h	height of porous micropillar used in VOF simulation (m)
L	characteristic length
n	mode of characteristic length
P	micropillar pitch (m)
p	pressure (Pa)
$\Delta p_{La,max}$	maximum Laplace pressure
$\Delta p_{La,tot}$	total burst pressure
Q	volumetric flow rate (m^3/s)
R	radius of curvature of meniscus (m)
r	radius of curvature of pore edge (m)
$r_{droplet}$	radius of liquid droplets (m)
SE	Surface Evolver
TPL	triple phase contact line
t	time (s)
t_f	bursting time (s)
t_1	trench depth (m)
t_2	membrane thickness (m)
V	volume (m^3)
V	velocity (m/s)
We	Weber number ($2\rho VL/\gamma$)

Greek symbols

α	volume fraction
β	meniscus center-point angle (°)
γ	surface tension (N/m)
θ_a	apparent contact angle (°)
θ_y	intrinsic contact angle (°)
θ^*	critical contact angle (°)
κ	surface curvature (m^{-1})
μ	dynamic viscosity (Pa s)
ρ	density (kg/m^3)
τ	time constant for the oscillation of liquid droplet
φ	angular location of triple line (°)
ω	angle between the top surface and outer micropillar edge

Subscripts

f	fluid
g	vapor
La	laplace
l	liquid
la	liquid-air interface
NW	non-wetting
sl	solid-liquid interface
sa	solid-air interface
tot	total
W	wetting

prediction of burst Laplace pressure obtained under quasi-static condition (i.e., equilibrium thermodynamic analysis under low capillary number) is not applicable to highly dynamic flow conditions, where the liquid meniscus shape deformation by flow perturbation cannot be restored by surface tension force instantaneously. Therefore, the critical burst pressure is dependent on the liquid velocity and viscosity under dynamic flow conditions. A numerical simulation using Surface Evolver also predicts that surface defects along the outer micropillar edge can yield up to 50% lower Laplace pressures than those predicted with ideal feature geometries. The liquid retention strategy developed here can facilitate the routing and phase management of dielectric working fluids for application in heat exchangers. Further improvements in the retention performance can be realized by optimizing the fabrication process to reduce surface defects.

1. Introduction

Porous structures with the capacity to retain low surface tension liquids (e.g. dielectric refrigerants, oils) against an imposed pressure difference are increasingly needed in many applications, including oil transportation [1], water/oil separation [2,3], microfluidics [4], and thermal management of micro/power electronic systems [5]. In the microelectronics industry, increasing performance demands necessitate both more memory and more central and graphics processing unit (CPU and GPU) cores, resulting in increased device density and consequent thermal management challenges. Likewise, for power electronic systems, gallium nitride (GaN) high-electron-mobility transistors (HEMT) can improve the performance of radar amplifiers, hybrid/electric vehicles, and LED arrays; however, thermal limitations prevent full exploitation of this technology, where transistor-level power densities can exceed 10 kW cm^{-2} [6]. For these applications, thin-film evaporative cooling in porous media (<40 μm) with a small pore size (<5 μm) can enable high heat transfer coefficients, exceeding

10^6 W m^{-2} K^{-1} at operating temperatures <100 °C [7–9]. However, this performance requires stable liquid-vapor interfaces in porous structures. A stable liquid-vapor interface can greatly benefit from low surface tension liquid retention in these structures under pressure, which is currently a challenge.

This problem is especially important for data centers, which represent about 2% of U.S. electricity consumption and are responsible for 2% of global CO$_2$ emissions (similar to the aviation carbon footprint), [10,11]. In particular, the miniaturization of computing systems and electronic circuits has culminated in three-dimensional (3D) stacked chips for high-end servers. Though offering dramatic manufacturing and electrical design advantages, this approach poses significant thermal problems in the implementation of high-performance 3D integrated circuits (3D ICs) with power densities that will soon exceed 5 kW cm^{-2} [12]. As a potential solution, interlayer two-phase evaporative cooling is considered a promising approach for heat removal, but it requires dielectric working fluids to avoid the difficulties associated with water in direct contact with microelectronic devices [13].

Despite the potential of dielectric liquids, most previous studies have been limited to microheat exchangers that use water as a working fluid. Previous studies have reported that venting vapor bubbles from water in microchannels through hydrophobic membranes can improve flow stability and facilitate heat transfer at the solid-liquid interface [14–16]. While thin-film evaporative microheat exchangers integrated with nanoporous alumina membranes have demonstrated heat flux removal up to 0.6 kW cm^{-2} [14], more recent studies have shown thin-film porous copper structures with heat flux removal exceeding 1 kW cm^{-2} with superheat <10 K using water, as well as the potential to implement phase separation using liquid retention membranes [9,17]. Despite the recent advances in phase routing microheat exchangers using water as the working fluid, mechanisms for maintaining stable liquid-vapor interfaces for low surface tension liquids (i.e., γ < 0.015 N/m) are lacking.

However, there have been many recent efforts to design non-wetting surfaces for non-polar hydrocarbon-based liquids [18–21] (i.e., superoleophobic or superomniphobic). Naturally occurring superoleophobic surfaces in air have been observed on Springtails (Collembola Entognatha), a wingless arthropod which lives in soil, decaying material, and on plants [22]. Their surface is composed of hierarchical structures of nanoscopic interconnected granules with re-entrant curvature, which prevents them from suffocation while immersed in polar and non-polar liquids. Thus, recent bio-inspired surfaces show that with a combination of proper surface texturing and sustaining a low solid fraction [1,23,24], it is possible to tune substrate wettability, even for low surface tension liquids [18,20,25]. Superoleophobic surfaces have been designed to yield both high and low contact angle hysteresis, (CAH) [26,27], and recent studies have shown non-wetting surfaces for fluorinated-carbon based liquids, which have some of the lowest measured surface tensions [20,28]. Despite the progress in development of non-wetting surfaces for non-polar liquids, there has been no demonstration of low surface tension liquid retention behind porous membrane structures against a pressure difference across the membrane.

Capillary stop valves have been used in biochemical systems for retaining wetting liquids against a driving pressure [29–32]. In these structures, a sudden expansion of the capillary cross-section stops the liquid from further advancing along the channel. While capillary stop valves have been shown to restrict the advance of aqueous liquids containing surfactants [29,33–36], they have not been demonstrated to pin non-polar liquids. However, the meniscus pinning approach applied in these systems holds promise for low surface tension liquids. Most recently, we have shown contact line pinning of non-polar liquids using glass capillary structures, which allow for liquid menisci to transition from concave to convex and do not permit flow, despite pressurization of the liquid [28].

In this work, we develop a novel approach for retaining low surface tension liquids behind a porous membrane by means of the design of silicon micropillar structures on its surface. The liquid retention and bursting behavior is identified by experimental visualization as well as pressure tracing. An analytical model is developed to predict the pressure of the liquid meniscus with a 3D capped spherical shape before and after bursting, based on calculating the total free energy change during the process. The analysis provides an in-depth understanding of the physics as liquid advances along the porous micropillar, which comprises five flow regimes: (1) wicking through the inner channel of the micropillar structure, (2) pivoting from a concave to convex shape along the inner micropillar edge (only for high surface tension liquids), (3) expansion to a hemispherical cap along the outer micropillar edge, (4) expansion of the meniscus beyond a hemisphere along the outer micropillar edge, and (5) bursting of the meniscus, where

the contact line advances along the outer surface of the micropillar. Because the analytical model considers only structures with perfectly sharp edges and quasi-static conditions, a transient computational model using ANSYS-Fluent is performed to predict the dynamic behavior of the meniscus and explore the associated dynamic effect on liquid pinning pressure under different flow rates [37]. Surface defects along the outer micropillar edge are considered separately by using a computation model employing Surface Evolver and Comsol Multiphysics, which predicts the static meniscus shape by computing the minimum surface energy, using a gradient-descent method [38]. To our knowledge, this paper presents the first approach to retaining liquids with small equilibrium contact angles, such as dielectric liquids (i.e. fluorinated compounds), using microfabricated micropillar structures. This approach can aid in phase management related applications that require stable liquid-vapor interfaces [39].

2. Theoretical analysis

Fig. 1 illustrates the action of the porous micropillar structure in retaining liquid and shows the contact line dynamics for a wetting liquid as it advances toward the external orifice. For very low surface tension (e.g., non-polar) liquids, the meniscus initially wicks through the inner channel of the micropillar and immediately spreads along the top surface, as shown in Fig. 1(k)–(n). After advancing to the outer micropillar edge, the meniscus is pinned and forms a hemispherical shape corresponding to the maximum Laplace pressure, as shown in Fig. 1(p). The pressure barrier formed is attributed to the change in meniscus interfacial area. A resistive capillary force opposes any increase in surface area and therefore total interfacial energy, and prevents the meniscus from further expansion [32–34]. A convex meniscus implies a positive pressure of the wetting liquid with respect to the non-wetting phase (i.e., p_W > p_{NW}). While the contact line of the meniscus is pinned at the outer edge, the apparent contact angle, θ_a, (between the top micropillar surface and meniscus liquid-vapor interface) increases from the intrinsic contact angle of the liquid and micropillar material, θ_y, until it reaches the critical angle, θ^*, which corresponds to the advancing contact angle with respect to the outer edge of the micropillar structure, as shown in Fig. 1(j). A bursting event corresponds to when the apparent contact angle exceeds the critical angle (Fig. 1(j)), and the liquid advances along the outer micropillar edge. The phenomenon related to meniscus pinning is known as the canthotaxis effect, and was originally presented by Gibbs for thermodynamically describing the resistance of wetting liquids spreading along sharp edges [40]. While a molecular understanding of such a characteristic is still unclear, recent studies [41,42] have demonstrated thermodynamically that once the liquid wets the sharp edge, the system will always be at its minimum energy state until the contact angle at sharp edge exceeds the critical value $\theta^* = \omega + \theta_y$, where ω is the angle between the top surface and outer micropillar edge (e.g., 90° in this study). Therefore, a liquid with higher intrinsic contact angle (i.e., higher solid-liquid interfacial energy) will be pinned more stably at the edge. That is to say, for liquids with infinitesimal intrinsic contact angles, the maximum bursting pressure can be approximated as $\theta^* = 90°$, yielding a hemispherical meniscus shape. For liquids with finite equilibrium contact angles (i.e., lower solid-liquid interfacial energy), the meniscus can be expanded beyond a hemispherical shape that corresponds to $\theta^* = 90° + \theta_y$. In this case, the pressure at burst does not correspond to the maximum Laplace pressure, but is lower.

The wicking, pinning, and bursting behavior of liquid along the porous micropillar structure can be analyzed theoretically using a free energy approach with a quasi-static assumption [32,33,41,42].

High Surface Tension Liquids

Low Surface Tension Liquids
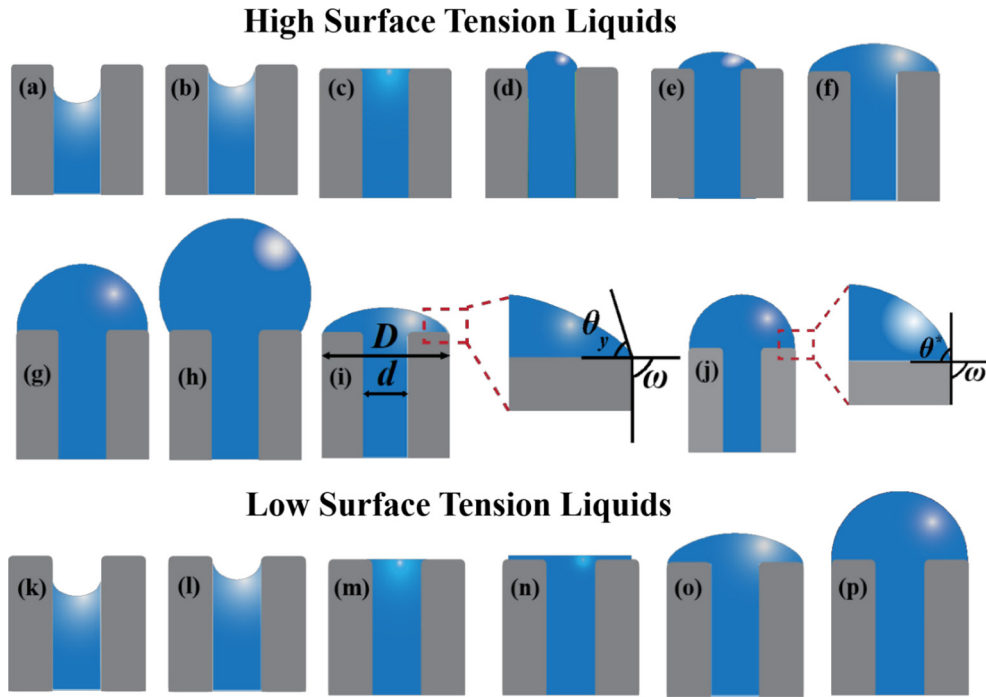
Fig. 1. Liquid pinning on porous silicon micropillar structures: Liquid initially wicks through the inner channel of the micropillar structure as shown in images (a) and (k). Liquid then pins along the inner micropillar edge ((b) and (l)). For high surface tension liquids, a convex meniscus is formed along the inner micropillar structure (d), then advances along the top micropillar surface (e). For low surface tension liquids, the meniscus immediately advances to the outer micropillar edge (n). For all liquids, the meniscus is pinned along the outer micropillar edge as shown in images (f) and (o). With increasing liquid pressure, the meniscus continues to expand to a hemispherical shape that yields a minimum radius of curvature and maximum Laplace pressure ((g) and (p)). The meniscus expands until it forms a critical angle, θ^*, at which point depinning at the liquid contact line occurs and the meniscus advances along the outer micropillar edge, which is termed "burst". Bursting coincides with the hemispherical meniscus for low surface tension liquids, but high surface tension liquid can sustain stable menisci with volumes exceeding a hemisphere.

A schematic and the dimensions of the structure are shown in Fig. 2. The advancement of liquid along the porous micropillar can be described in terms of the total free energy as

$$E_{tot} = E_{sl} + E_{sa} + E_{la} = A_{sl}\gamma_{sl} + A_{sa}\gamma_{sa} + A_{la}\gamma_{la} \qquad (1)$$

where the surface tension γ_{sl}, γ_{sa}, and γ_{la} are correlated by Young's equation as

$$\gamma_{sa} = \gamma_{sl} + \gamma_{la} \cos \theta_y \qquad (2)$$

The corresponding pressure in the liquid associated with the change in total free surface energy can then be obtained by taking the derivative of Eq. (1) with respect to the liquid volume and substituting Eq. (2), which gives

$$\Delta p = -\frac{dE_{tot}}{dV_l} = \gamma_{la}\left(\cos \theta_y \frac{dA_{sl}}{dV_l} - \frac{dA_{la}}{dV_l}\right) \qquad (3)$$
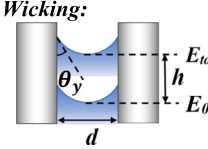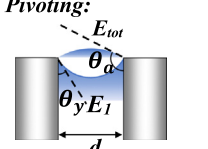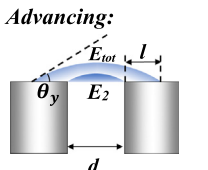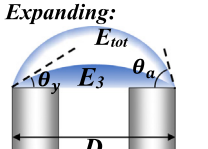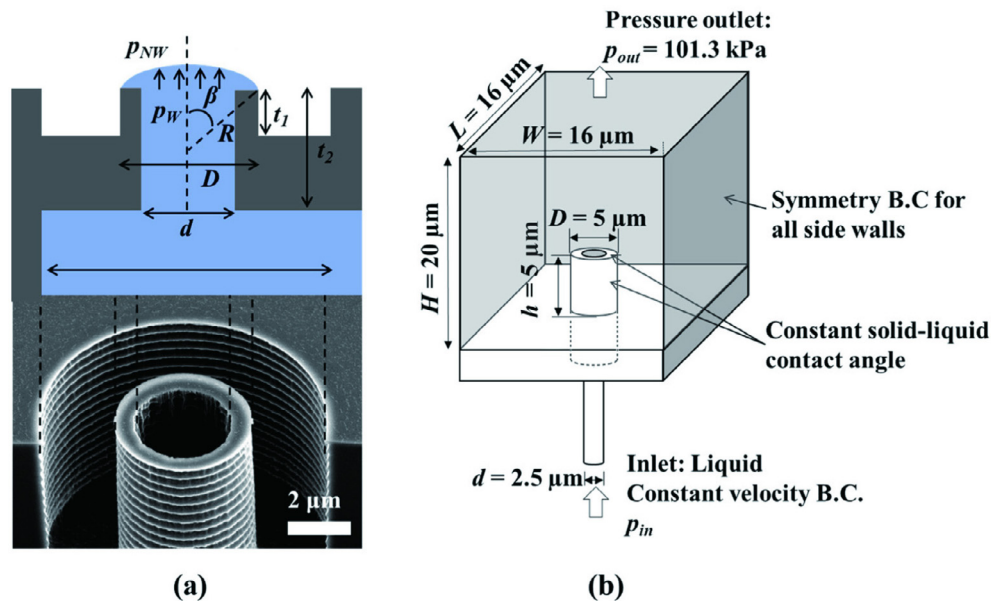

Fig. 2. (a) Schematic of the theoretical model geometry (top) for a micropillar and scanning electron micrograph of a fabricated micropillar (bottom). (b) Computational domain for transient simulations of the micropillar structure.

During the process of liquid penetrating through the micropillar structure, the change of total free surface energy and liquid volume at different stages (e.g., wicking, pivoting, advancing, and expanding) can be calculated using the associated geometric boundary conditions, assuming that the meniscus maintains the geometry of a capped sphere:

3.1. Quasi-static modeling – Surface Evolver

The critical pinning pressures of water on perfect and defective micropillars are studied using a quasi-static approach *via* Surface Evolver [38]. Surface Evolver is a surface energy minimization program with geometrical constraints such as vertex (or edge)

Wicking:

$$E_{tot} = E_0 - \pi dh\gamma_{la}\cos\theta_y \tag{4}$$

$$V_{tot} = V_0 + \frac{\pi}{4}d^2 h \tag{5}$$

Pivoting:

$$E_{tot} = E_1 - \frac{\pi d^2}{2}\left(\frac{1-\sin\theta_y}{\cos^2\theta_y} - \frac{1-\sin\theta_a}{\cos^2\theta_a}\right)\gamma_{la} \tag{6}$$

$$V_{tot} = V_1 + \frac{\pi d^3}{24}\left[\frac{(1-\sin\theta_y)^2(2+\sin\theta_y)}{\cos^3\theta_y} - \frac{(1-\sin\theta_a)^2(2+\sin\theta_a)}{\cos^3\theta_a}\right] \tag{7}$$

Advancing:

$$E_{tot} = E_2 + \pi(l^2 + dl)\left(\frac{2-2\cos\theta_y}{\sin^2\theta_y} - \cos\theta_y\right)\gamma_{la} \tag{8}$$

$$V_{tot} = V_2 + \frac{\pi(1-\cos\theta_y)^2(2+\cos\theta_y)}{24\sin^3\theta_y}[(d+2l)^3 - d^3] \tag{9}$$

Expanding:

$$E_{tot} = E_3 + \frac{\pi D^2}{2}\left(\frac{1-\cos\theta_a}{\sin^2\theta_a} - \frac{1-\cos\theta_y}{\sin^2\theta_y}\right)\gamma_{la} \tag{10}$$

$$V_{tot} = V_3 + \frac{\pi D^3}{24}\left[\frac{(1-\cos\theta_a)^2(2+\cos\theta_a)}{\sin^3\theta_a} - \frac{(1-\cos\theta_y)^2(2+\cos\theta_y)}{\sin^3\theta_y}\right] \tag{11}$$

Combining Eqs. (4)–(11) and substituting them in Eq. (3) allows for theoretical prediction of the pressure variation as liquid flows through the porous micropillar and gets pinned along the sharp edge. After the critical contact angle is formed along the micropillar edge, the liquid eventually collapses. Since the edge angle $\omega = 90°$, a spherical drop profile cannot be satisfied during the collapse as the micropillar edge will protrude into the liquid outline. Therefore, the liquid bursts suddenly and spreads instantaneously down the side of the micropillar, where the contact line splits into a capped sphere sitting on the top of the micropillar and a falling film surrounding the outer micropillar wall [41]. Such a process is highly non-equilibrium and tracing the free energy is difficult due to the irregular shape deformation. However, once liquid burst is over, no additional pressure barrier is present and the flow is again dominated by the contact line friction as the liquid spreads freely on the whole substrate. The corresponding liquid pressure variation after the burst can then be calculated, again using the change in free energy, by equations 8 and 9, using an initial diameter of $D = 5 \mu m$.

3. Computational simulation

The pinning and bursting behaviors of two different working fluids (water and FC-40) are studied using both a quasi-static and a dynamic simulation method. Comparing the results from the different computational tools allows for determination of the flow regions under which the dynamic effect would impact the liquid retention performance of the porous micropillar structure.

position and contact angle, and constraints on integrated quantities such as fluid volume. The Evolver generates a static liquid meniscus shape by minimizing the total surface energy of the meniscus down the energy gradient for the given constraints, from which a corresponding Laplace pressure can be determined by calculating the surface mean curvature, κ. Since Surface Evolver cannot capture dynamic behavior such as liquid burst, the critical pinning point is determined iteratively by first obtaining the equilibrium liquid shape with a fixed volume and then examining the contact angle at the micropillar edge. Starting with a small volume of liquid droplet on the top surface of the micropillar, the surface energy minimization is performed iteratively with a small increment in volume until the contact angle at the equilibrium state reaches the burst criterion – i.e., $\theta^* = 90° + \theta_y$. The liquid droplet volume corresponds to the critical burst volume and the associated burst pressure is obtained from the Young-Laplace equation using the minimum mean curvature. Details of the Surface Evolver simulation can be found in Supplementary Material (Appendix A).

3.2. Dynamic modeling – Volume of fluid (VOF) simulation

A transient three-dimensional simulation model using the Volume of Fluid method (VOF) is developed to predict the liquid pressure and capture the contact line dynamics as the meniscus advances from the inner channel to the outer edge of the porous micropillar structure. The simulation tracks the evolution of the meniscus and corresponding pressure profile as the meniscus moves to different locations along the micropillar structure.

Table 1
Input parameters and modeling setup for numerical simulation.

Input parameters	Value			
Outer diameter, D	5 µm			
Inner diameter, d	2.5 µm			
Micropillar height, h	5 µm			
Membrane width,	16 µm			
Liquid inlet temperature, T_{in}	293 K			
Liquid inlet Mass flow rate, $\dot{m}_{in}$		2×10^{-10} kg/s	2×10^{-9} kg/s	1×10^{-8} kg/s
Ca number		0.001	0.01	0.05
Outlet gauge pressure, p_{out}	0 kPa			
Properties	Water		FC-40	
Surface tension	7.3×10^{-2} N/m		1.6×10^{-2} N/m	
Viscosity	1.0×10^{-3} kg/m-s		4.1×10^{-4} kg/m-s	
Membrane contact angle	10°		3°	
Solution methods	Setup			
Number of meshes	0.8 million hexahedral meshes			
Surface tension modeling	Continuous Surface Force (CSF)			
Pressure-Velocity Coupling	Pressure Implicit with Splitting of Operator (PISO)			
Spatial discretization	Gradient		Green-Gauss Node Based	
	Pressure		PREssure STaggering Option (PRESTO!)	
	Momentum		Second Order Upwind	
	Volume Fraction		Geo-Reconstruct	
Time Stepping Method	Variable		Global Courant = 2	

The VOF model [43,44] employs one set of governing equations to solve for the liquid and vapor domains, using ANSYS Fluent [45]. The computational solver is implemented to compute the conservation equations below:

Continuity:

$$\frac{\partial \alpha_k}{\partial t} + \nabla \cdot (\alpha_k \vec{V}) = 0, \qquad (12)$$

Momentum:

$$\frac{\partial}{\partial t}(\rho \vec{V}) + \nabla \cdot (\rho \vec{V} \vec{V}) = -\nabla p + \nabla \cdot \left[\mu (\nabla \vec{V} + \nabla \vec{V}^T) \right] + \rho \vec{g} + \vec{F}, \qquad (13)$$

where α_k, ρ, μ, and $\vec{F}$ are the phase volume fraction, density, dynamic viscosity, and body force terms, respectively. The interfacial forces are modeled using the Young-Laplace equation:

$$\vec{F}_\gamma = \gamma \kappa \nabla \alpha \qquad (14)$$

where γ and κ are the surface tension and surface curvature, respectively. The change in momentum due to the interfacial forces is expressed using the Continuous Surface Force (CSF) model [46]:

$$\vec{F}_\gamma = \gamma \kappa \frac{\rho}{\rho_f + \rho_g} \nabla \alpha \qquad (15)$$

Fig. 2(b) shows the three-dimensional computational domain used for the simulation. In this model, a micropillar structure is considered, with an inner diameter, outer diameter, and thickness of 2.5 µm, 5 µm, and 25 µm, respectively.

In this model, grid independence is established using a 3D unstructured hexahedral mesh with three different mesh sizes. The coarsest mesh has 0.3 million computational nodes in the domain and is refined twice, up to 2.1 million hexahedral nodes. A mesh sensitivity analysis is performed by monitoring local pressure values at the inlet and outlet of the computational domain. The final mesh generated has a comparatively modest 0.8 million nodes, which minimizes computational effort. There is only a minimal pressure difference (≤1.3%) between the finest mesh size and the meshes implemented for these studies. The micropillar structures are periodically arranged, and therefore symmetric boundary conditions are used for all sidewalls. An inlet boundary velocity is

determined based on a capillary number, Ca, at the micropillar inlet. In order to explore if the dynamic effects (e.g., viscous and inertial effects) are significant in the liquid pinning performance, three different inlet conditions were chosen for the study, with Ca number = 0.001, 0.01, and 0.05. The surface tension, γ, is assumed to be constant, and a constant pressure outlet boundary condition is applied at the outlet. Details of the input parameters, fluid properties, and solution methods for numerical modeling are summarized in Table 1. The maximum Laplace pressure is calculated by subtracting the viscous effects from the total pressure drop predicted using the Hagen-Poiseuille equation:

$$\Delta p_{viscous} = \frac{128 \mu h Q}{\pi d^4} \qquad (16)$$

4. Materials and methods

4.1. Design and microfabrication of porous silicon micropillar structures

To retain both polar and non-polar liquids, we applied microfabrication techniques to create a membrane containing an array of porous silicon micropillar structures with re-entrant surface features. The design and key parameters of the porous micropillar structures are shown in Fig. 3: D is the outer micropillar diameter, d is the inner micropillar diameter, D_t is the trench diameter, t_1 is the trench height, t_2 is the channel height, and P is the pitch, defined as the center-to-center distance between adjacent micropillars. The porous micropillar structures were constructed using two front-side deep reactive ion-etching (DRIE) steps to independently delineate trenches and through-holes. An additional back-side DRIE step followed to define the membrane thickness. The inner diameter of the micropillars was limited by the resolution of both the lithography and the DRIE steps, which required a high aspect ratio through-hole. Therefore, the micropillar inner diameter was selected as 3 µm, the thickness was selected as 0.7 µm, and the corresponding outer diameter was 4.4 µm. The area of the micropillar arrays fabricated here was 1 mm². The DRIE etch produced sharp edges at the intersection of the outer and top surfaces of the micropillars (i.e., angle $\omega \geqslant 90°$ as defined in Fig. 1), which are beneficial for pinning liquids with infinitesimal intrinsic
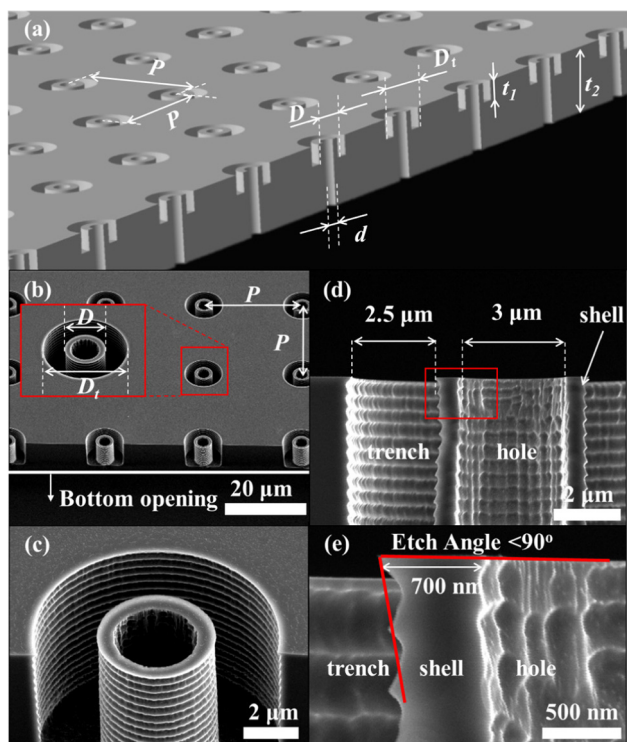
Fig. 3. Schematic and scanning electron micrographs of the porous micropillar structures fabricated and studied here. (a) Schematic representation of an array of micropillar structures. The geometrical features of the porous micropillars include the outer diameter, D; inner diameter, d; trench diameter, D_t; trench height, t_1; trench depth, t_2; and pitch, P, defined as the center-to-center distance between adjacent micropillars. (b) Scanning electron microscopy (SEM) image of oblique top view of the square array of micropillars with a pitch of $P = 25\ \mu m$. (c) Oblique top view of a single micropillar. (d) Cross-sectional view of a single porous micropillar. (e) Magnified cross-sectional view of the micropillar, confirming the thickness of $0.7\ \mu m$. The outer corner of the micropillar has an etch angle less than $90°$ which allows lower surface tension liquids to maintain a hemispherical shape along the outer micropillar edge with diameter, D.

contact angles. See Supplementary Material for microfabrication process details (Figs. B1 and B2).

4.2. Laplace pressure measurement apparatus

Using the fabricated devices, we experimentally measured the pressure difference sustained across the membrane, Δp_{La}, before and after liquid burst (i.e. $\Delta p_{La,max}$) through the porous micropillar structures. Pressure measurements were accompanied by simultaneous visualizations of the menisci using an optical microscope (Nikon Eclipse 80i) with a Plan Fluorite objective having a numerical aperture (NA) of 0.15. The pinning and bursting events were visualized from the top of the membrane surface and recorded using a CCD camera (Thorlabs DCC1545M), as more fully described in Supplementary Material (Appendix C). The setup included a programmable syringe pump (Harvard PHD 2000) which pumped liquid through stainless steel tubing (IDEX) with an inner diameter of $62.5\ \mu m$, connected in series with two different pressure transducers, one (Omega PX419) with a 0–250 psig range for water, and another with a 0–5 psig range for FC-40 (see Appendix C in Supplementary Material). In order to achieve an ultra-small liquid flow rate, the syringe was first partially filled with certain volume of air by pulling up the piston in ambient atmosphere before drawing in the working fluid. Then, the syringe containing the liquid-air mixture was assembled on the syringe pump for injecting the liquid. Such an approach reduced the sensitivity of the system pressure to volume changes, but allowed the pump to deliver a finely

controlled liquid volume to the device, below the minimum pumping rate specified by the syringe pump manufacturer. All pressure measurements were referenced to the ambient pressure prior to initiation of the flow. The nominal flow rate at the syringe pump used for all experiments was 0.4 ml/min. This nominal flow rate primarily corresponded to compression of gas in the inactive parts of the system (a far lower actual flow rate was delivered to the membrane). The liquids used for these studies were deionized (DI) water and FC-40 (Sigma-Aldrich, St. Louis, MO, USA, CAS Number: 51142-49-5).

5. Results and discussion

5.1. Theoretical analysis under quasi-static condition

Fig. 4 shows the analytically predicted liquid free energy and pressure variation as liquid flows through a single porous micropillar. The meniscus initially wicks through the micropillar structure, which leads to a constant increase in the solid-liquid interfacial area and a decrease in the liquid-air interfacial area. Since the interfacial energy between the solid and liquid is far smaller than that between the liquid and air, there is a constant decrease in total free energy, which corresponds to a constant negative Laplace pressure, as shown in Fig. 4(b), point (i). As the meniscus flows
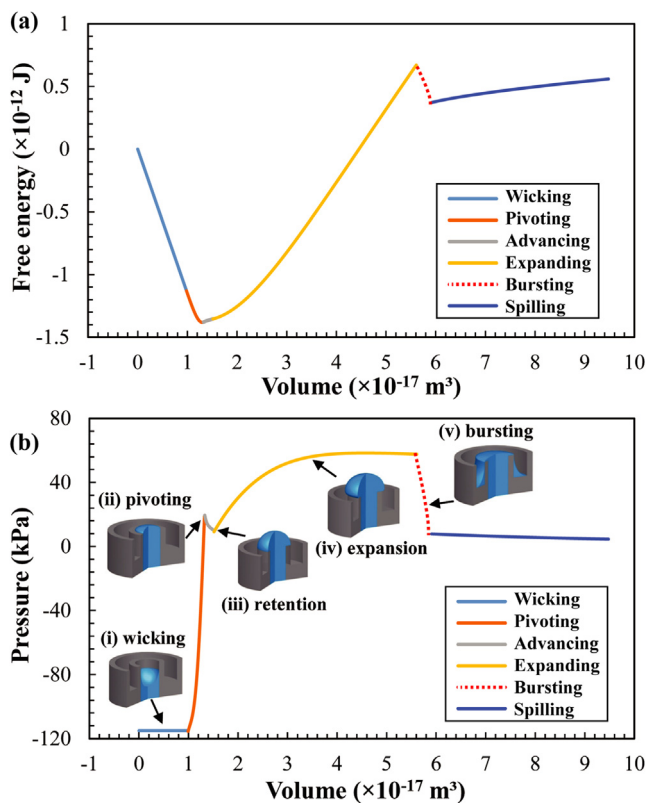

Fig. 4. Analytical predictions of (a) free energy and (b) liquid pressure variation during the wicking, pivoting, advancing, expanding, and free spreading (post-burst) of water through the porous micropillar structure. The predictions were made based on a quasi-static assumption which neglects any viscous, gravitational, or other dynamic effects. The dotted red line represents the instantaneous bursting moment, accompanied by a sudden jump in liquid free energy and pressure. (i) Wicking through the inner micropillar structure (ii) Pivoting from a concave to convex shape along the inner micropillar edges (iii) Advancing along the top micropillar surface and pinning along the outer micropillar edge (iv) Expansion of the meniscus beyond a hemisphere along the outer micropillar edge and (v) Bursting (i.e., droplet collapse). (For interpretation of the references to color in this figure legend, the reader is referred to the web version of this article.)

to the top micropillar surface, it pins along the inner micropillar edge with an inner diameter, d. At this point, the meniscus pivots from a concave to convex shape, which results in a transition from negative to positive Laplace pressure, as shown in Fig. 4(b), point (ii). After formation of the intrinsic contact angle, θ_y, with respect to the top micropillar surface, a discernable pressure drop occurs. This pressure drop is attributed to the advance of the contact line from the inner edge toward the outer edge, during which an increase in the radius of curvature leads to reduced Laplace pressure across the liquid-vapor interface, as shown in Fig. 4(b), point (iii). Once liquid wets the edge, an increase in liquid pressure is observed due to the increase in the contact angle. The maximum pressure is obtained when the liquid forms a hemisphere, as shown in Fig. 4(b), point (iv). As liquid expands further beyond a hemisphere while being pinned on the edge, a slight decrease in pressure is observed due to increase in radius of curvature. Once the burst criterion is reached as shown in Fig. 4(b), point (v), the liquid collapses spontaneously and a sharp decrease in pressure is observed. A small pressure is required to drive the liquid to spread freely on the substrate.

5.2. VOF simulation with dynamic effects

Fig. 5 illustrates VOF simulation results for water, showing the evolution of the meniscus and the corresponding capillary pressure at different micropillar locations under three flow rates. The pressure response shown in Fig. 5(a) reveals similar trends in pressure variation, as predicted from quasi-static analytical calculations, in which the wicking, pivoting, advancing, and expansion stages are delineated clearly by changes in pressure. The fluctuations in the pressure signal are attributed to perturbation and instability during volume growth. Nevertheless, with increasing flow rate, there is a considerable increase in the liquid pressure due to the intensified viscous pressure. If the viscous pressure drop is subtracted based on Hagen-Poiseuille flow, the critical bursting pressure can be obtained, as shown in Table 2. The results reveal that when the flow rate is increased by 10 and 50 times, the burst Laplace pressure is reduced by 8.6% and 53%, respectively. They further suggest that the results obtained with the quasi-static assumption will no longer hold for high Ca flow and that the critical burst criterion is dependent on the liquid velocity.

Fig. 5(b) shows the geometric evolution (i.e., mean curvature and apparent contact angle) of the liquid droplet, starting with a flat liquid meniscus (in the middle of the pivoting stage) and ending with liquid burst. It is evident from the difference in critical contact angle that the shapes of the liquid menisci at the burst points deviate from a capped sphere. A decrease in the mean curvature, κ, is also observed for high Ca flow, which corresponds to a lower Laplace pressure. The decrease is particularly significant for $Ca = 0.05$, where the mean burst curvature is reduced from 0.35 μm^{-1} to 0.28 μm^{-1}. It is also observed in Fig. 5(c) that the liquid expands to a larger critical volume before bursting under the higher flow rate (i.e., high Ca number). This finding suggests that at sufficiently high flow rates, the surface tension force is no longer strong enough to instantly restore the shape of the liquid meniscus to its equilibrium condition. Therefore, the liquid will undergo an anisotropic expansion with a higher growth rate in the vertical direction, during which the surface energy is no longer at its minimized value. Such a dynamic effect can be quantitatively analyzed by calculating the change in liquid volume within the time constant, τ, associated with the shape restoration by surface tension. Considering the perturbation of a liquid droplet held together by surface tension, the frequency of the nth oscillation mode in air is given by [47]
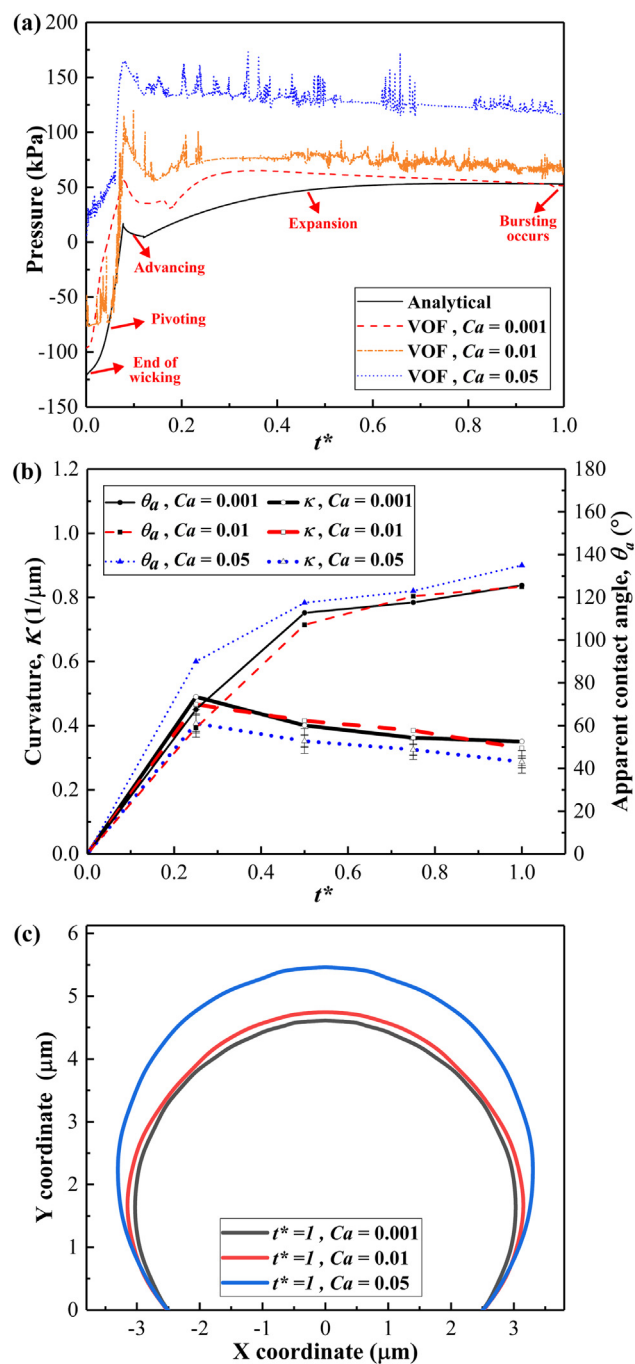

Fig. 5. (a) Comparison of pressure trace curves from VOF simulations under different flow rates (Ca numbers) with analytical prediction obtained with quasi-static assumption. The time is normalized, with pivoting starting at $t^* = 0$ and the bursting occuring at $t^* = 1$. (b) Variation of mean curvature and apparent contact angle of liquid meniscus under different flow rates (Ca numbers). The time is non-dimensionalized, with an initially flat meniscus (curvature equals to zero) at $t^* = 0$ and liquid bursting at $t^* = 1$. (c) The shape of the meniscus when burst happens under three different Ca flow. The inconsistency in the liquid profile and pressure during the process under three flow rates suggests that burst behavior cannot be described solely by quasi-static analysis.

Table 2
Maximum bursting pressure for three different Ca numbers, using water.

Capillary number	Viscous pressure (kPa)	Laplace burst pressure (kPa)	Total pressure (kPa)
0.001	1.9	51	52.9
0.01	18.7	46.6	65.3
0.05	93.4	23.9	117.3
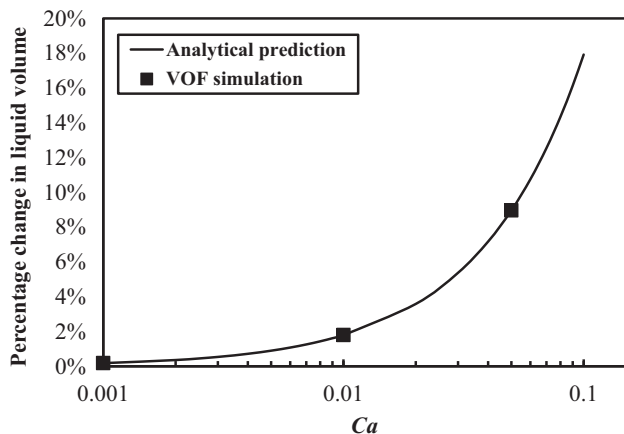
Fig. 6. Percentage change in liquid volume as a function of capillary number within a time period τ that is required for the droplet to restore its deformed surface geometry to the equilibrium shape (i.e., a capped sphere) by the surface tension force. The quasi-static assumption that the droplet will always be at its local equilibrium condition becomes invalid under high Ca numbers, where the change in liquid volume becomes significant.

$$f = \sqrt{n(n-1)(n+2)\frac{\gamma}{\rho r_{droplet}^3}} \qquad (17)$$

where γ is the surface tension, ρ is the density, and $r_{droplet}$ is the radius of the droplet. Using water as an example with $r_{droplet} = 2.5\ \mu m$, the dominant mode of oscillation frequency ($n = 2$) is calculated to be $f_{n=2} = 6.11 \times 10^6$ Hz. Therefore, the time constant for the liquid to restore to its equilibrium shape from a small deformation is given by $\tau = 1/f_{n=2} = 0.16\ \mu s$. Fig. 6 illustrates the percentage change in liquid volume within the specified time constant τ for a liquid droplet with hemispherical geometry under different Ca numbers. The result shows that for Ca number of 0.001, 0.01 and 0.05 respectively, the liquid droplet undergoes

0.2%, 2% and 9% volume changes before its surface can be restored to an equilibrium spherical shape. Therefore, the liquid meniscus will not be able to maintain its minimum energy state during expansion under high Ca number conditions. The competing effects of the surface tension and the dynamic forces cause the liquid meniscus to oscillate in shape while expanding in volume, therefore resulting in different characteristics for the pressure traces and burst criterion. Since the deformation in meniscus geometry is stronger for high Ca number flows, the liquid droplet will exhibit greater burst volume, larger burst curvature κ, and smaller burst pressure under high flow conditions.

5.3. Experimental burst behavior

As discussed previously, the pressure/flow relationship as the meniscus advances through the membrane is influenced by quasi-static and dynamic effects and depends on the thermophysical properties of the liquid and flow rate. The flow rates required to perform burst pressure experiments in the capillary regime are too low to readily access ($Q_{water} = 2.4 \times 10^{-7}$ ml/min and $Q_{FC-40} = 1.2 \times 10^{-8}$ ml/min). We therefore conducted burst pressure experiments with a liquid-air mixture, using a syringe pump that supplied a constant plunger speed corresponding to a flowrate $Q = 0.4$ ml/min, but with a much smaller and variable flowrate supplied to the membrane (with the remainder accounted for by gas compression). Specifically, the syringe was filled with a portion of air prior to being filled with the liquid and assembled on the syringe pump, the pressure source. For all experiments, the liquid was initially close to the membrane surface before the system was pressurized by the syringe pump. When the syringe pump was turned on, the liquid immediately contacted the membrane, while the air within the inactive portions of the system started to be compressed and a pressure increase was observed. We observe no liquid leakage around the membrane surface during pressurization.

The liquid pinning and bursting behavior was directly visualized, as shown in Fig. 7. By converting the original videos to 4-bit
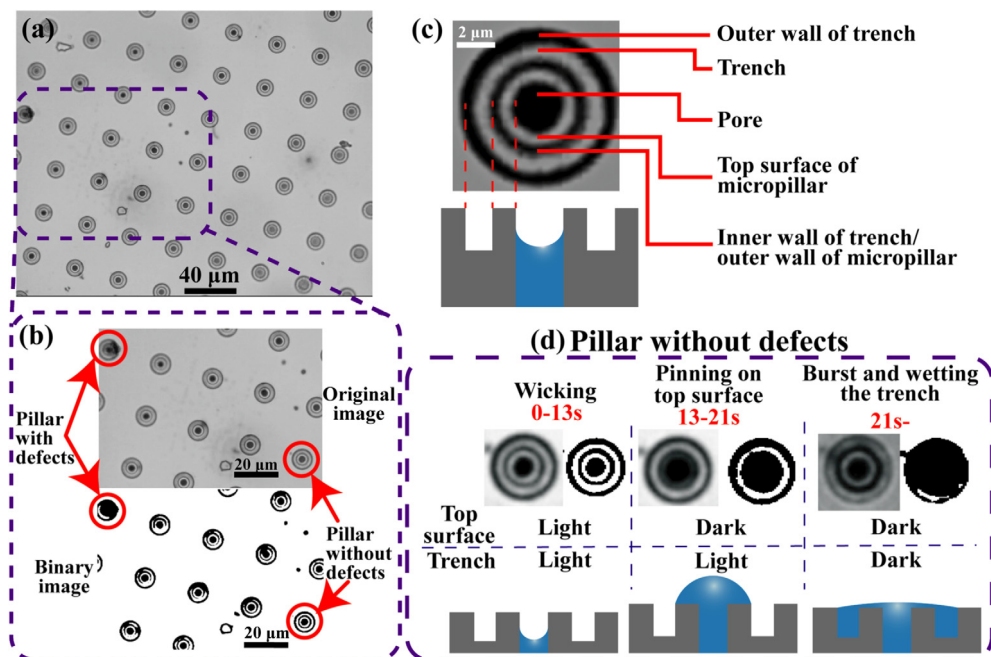
Fig. 7. (a) Optical image of the tops of the micropillars obtained from CCD camera (Thorlabs DCC1545M). (b) Original and binary images of micropillars with defects and without defects. (c) A schematic of a micropillar and corresponding part in the optical images. (d) Burst process of a micropillar without defects. The color of structure covered with liquid will turn dark. (For interpretation of the references to colour in this figure legend, the reader is referred to the web version of this article.)
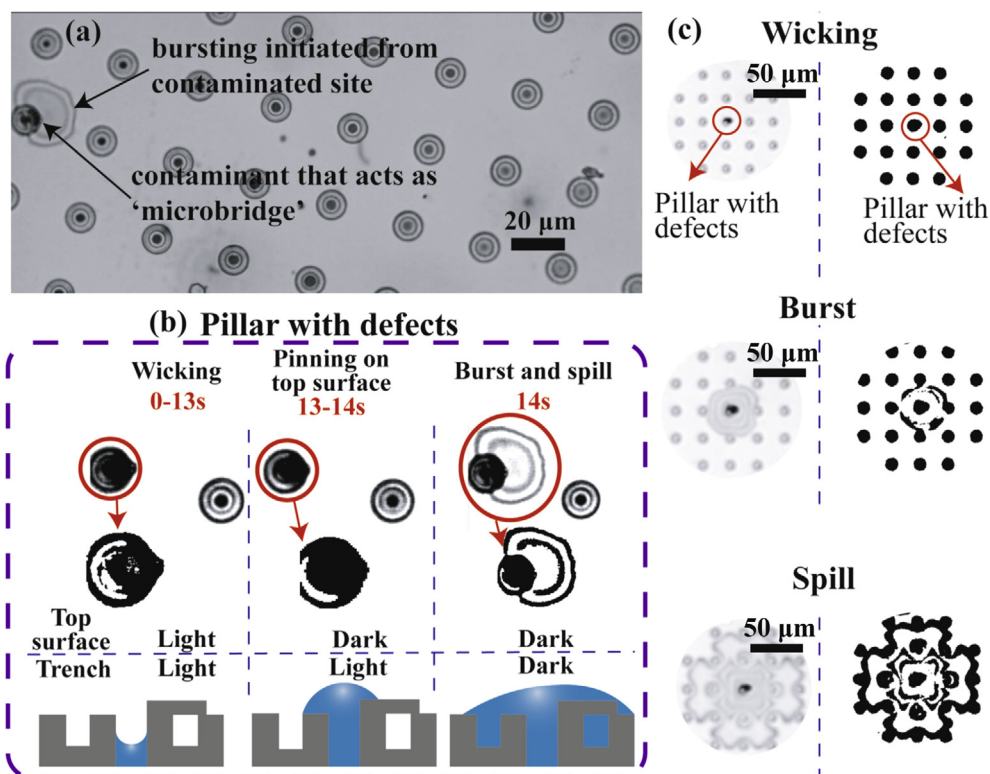
Fig. 8. (a) Early-bursting initiated from contaminated sites. $\Delta p_{La,max}$ for early-bursting events are less than 50% of the predicted theoretical values for both FC-40 and water. The contaminant acts as a 'microbridge' for liquid to wick to adjacent micropillars, which yields lower pressures than predicted. (b) 4-bit grey scale and binary images of the burst process of a micropillar with defects. The structure covered with liquid will turn dark. (c) Zoomed-out view demonstrating liquid bursting and spilling from a single micropillar with a defect.

grayscale images, pellucid views of the wicking, pinning, and bursting process were obtained that allow for identification of the wetted and non-wetted regions from light contrast at different locations. When the liquid is wicking through the inner channel of the micropillar, the top surface and trench have not been covered with liquid. Hence these regions exhibit a light color, while the pore area (with liquid wicking inside) is dark. As the liquid spreads over the top surface and gets pinned on the sharp solid edge, the whole top surface becomes dark due to a thick layer of liquid blocking the reflection. After liquid bursts from the edge, it spills into the trench, where the whole micropillar becomes dark. However, the top surface becomes slightly lighter again as the thick layer of pinned liquid becomes thinner after collapsing.

It was also observed in the experiments that the burst always occurs first at a single micropillar which has either a defect or contaminant. As shown in Fig. 8, surface contaminants and possible damage to the silicon micropillar structures occur in the micropillar array. These surface contaminants can act as 'microbridges' between the trench area of the micropillar structure and the top membrane surface, and allow liquid to wick along the top membrane surface and lead to local flooding around the micropillar trench area at much earlier time steps. Any further increase in volume causes the liquid to further advance to adjacent micropillars. As more volume of liquid is added, flooding occurs adjacent to neighboring micropillars. Fig. 8(b) shows a zoomed-out view when liquid bursts and spills from the contaminated side of the micropillar while it gets pinned on the outer edge of other defect-free micropillars. These defective micropillars act as pressure releasing valves that allow liquid to preferentially flow toward these 'openings' and penetrate the porous membrane with less resistance. Therefore, the overall pressure barrier is reduced due to the

presence of these defects, and the system-level liquid pinning performance is degraded significantly.

Experimental values of critical burst pressure $\Delta p_{La,max}$ using the micropillars fabricated in this study and glass capillary structures studied previously [28] are plotted against the micropillar outer diameter, D, ranging from 5 to 840 µm in Fig. 9(a). This plot confirms the Laplace pressure increases with decreasing D. The experimental values of $\Delta p_{La,max}$ for micropillar with an outer diameter of $D = 5$ µm versus liquid surface tension, as well as corresponding theoretical calculations and numerical simulations for an ideal micropillar geometry using Surface Evolver, are shown in Fig. 9(b) for $\gamma = 0.005$–0.1 N/m. The theoretical values of $\Delta p_{La,max}$ are calculated based on the Laplace pressure for an outer micropillar diameter, D, and $\theta^* = 90°$, based on the meniscus forming a spherical cap along the outer micropillar edge. While the simulation results from Surface Evolver and the theoretical results are in good agreement, the experimental values of $\Delta p_{La,max}$ are lower than theoretically predicted values for both FC-40 and water. Apart from the dynamic effects discussed in Section 5.2, we further attribute the lower measured Laplace pressures to the presence of surface contaminants and possible damage to the silicon micropillar structures, as shown in Fig. 8(a–c). These defects and contaminants cause local flooding at low liquid pressure, which results in an effective increase in micropillar diameter and further decrease of the pressure barrier for liquid retention. The effective max burst pressure then becomes smaller than the theoretical max burst pressure predicted, due to an increase in the effective outer diameter of the micropillar, as shown in Fig. 8(b). Thus, the applied pressure never rises as high as the predicted value for FC-40 and water. The effects of surface defects and surface contamination on the
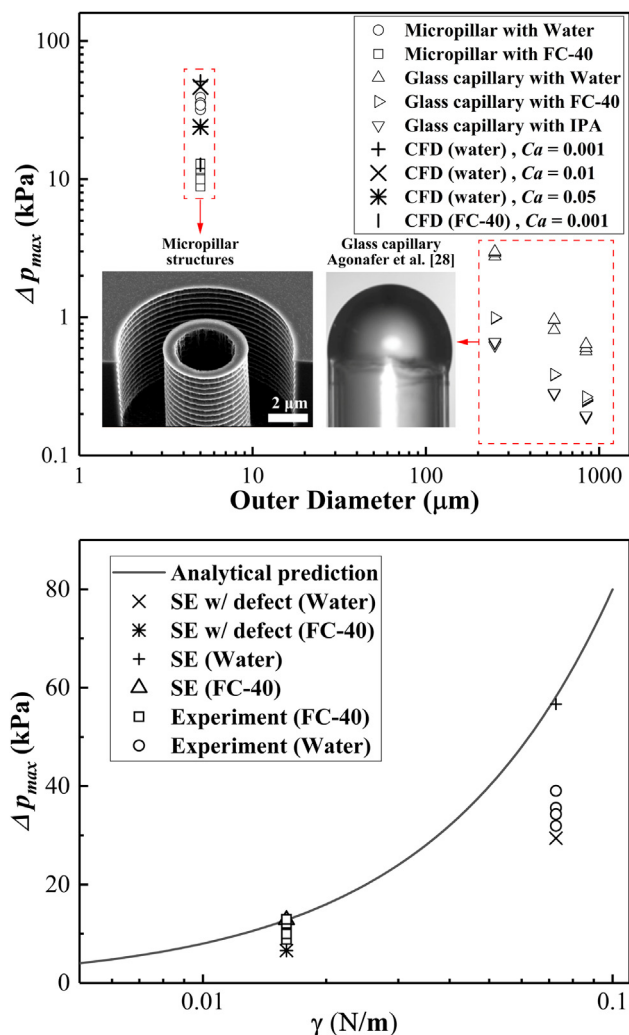
Fig. 9. Experimental, theoretical, and simulation results for $\Delta p_{La,max}$ (a) Experimental values of the maximum pressure for four different outer diameters for an array of micropillars and glass capillary structures [28]. (b) Experimental, theoretical, and numerical results for $\Delta p_{La,max}$ plotted against γ. Numerical results are obtained using Surface Evolver to predict the $\Delta p_{La,max}$ for micropillar structures with and without the presence of structural defects. See Supplementary Material (Appendix C) for more details.

maximum Laplace pressure can be accounted for using the simulation models, as discussed in the next section. Detailed pressure trace curves for both water and FC-40 can be found in Supplementary Material (Appendix D). The experimental measurements of transient pressure response do not agree with the theoretical and VOF simulations closely due to the presence of compressed air in the flowing channel. However, the critical burst pressure is in good agreement with the predicted values obtained in Surface Evolver for micropillars with defects, and by VOF simulations that predict dynamic effects (i.e., $Ca > 0.01$).

5.4. Effect of structural defects and surface contamination

The maximum Laplace pressure corresponding to a stable meniscus on a micropillar with a structural defect was determined using Surface Evolver [38] (see Supplementary Material Appendix A for detailed information). Results for these simulations are shown in Fig. 9(b). The Young-Laplace pressure was calculated for micropillars with a 5 µm outer diameter, D. In order to simulate surface defects along the outer micropillar edge, a 90° notch

2.75 µm deep was generated. The model predicts that the presence of structural defects along the outer edge of a micropillar can lead to a larger meniscus radius of curvature due to pinning of the liquid on the lateral wall along the structural defect. The $\Delta p_{La,max}$ for micropillars with structural defects are approximately 50% lower than the theoretically predicted values for both FC-40 and water, as shown in Fig. 9(b). These values corresponds closely with the experimentally measured values. For model validation, static liquid menisci shapes and corresponding pressures are also predicted for micropillars without the presence of defect sites. The model is within 4 percent of the analytical results for both FC-40 and water.

6. Summary and concluding remarks

In this study, we demonstrate liquid retention using an array of identical micropillar structures with re-entrant surface geometry. While such a geometry has been used for creating superoleophobic surfaces with strong liquid repelling characteristics in extensive studies [18–21,23–25,48–50], retention of low surface tension liquids behind porous membrane structures remains an unexplored area. Experimental visualization of the liquid advance along the porous micropillar array fabricated in this study reveals liquid pinning along the outer edge of defect-free micropillars and preferential liquid bursting from micropillars with defects or contaminants. An analytical model, based on free energy analysis with a 3D capped spherical geometry, was developed to predict the Laplace pressure as the shape of the meniscus on the micropillar structure evolves with increasing pressure. The expression takes a similar form to the models derived by Man et al. [32] and Chen et al. [33], but provides a more thorough analysis for describing the change in system pressure from wicking to bursting. Predications from the analytical model agree well with the results obtained from Surface Evolver for defect-free micropillars, but deviate from the experimental measurements of burst pressure by a significant margin. Two mechanisms were identified to elucidate this discrepancy, based on VOF simulation and Surface Evolver modeling. (1) Under high Ca number flow, the liquid meniscus deforms from its equilibrium geometry, therefore resulting in a higher liquid volume, larger radius of curvature, and smaller Laplace pressure before burst. This dynamic effect is intensified with increasing flow rate, which leads to attenuated liquid retention under high flow rate. (2) Contaminants and structural defects create microbridges that allow liquid to spread to local neighbor regions at low liquid pressure, which reduces the pressure barrier for liquid bursting from the porous micropillar array. These effects provide new insights into the classical understanding of liquid pinning along a sharp edge, developed based on a quasi-static assumption [40–42,51]. With these effects, the study demonstrates maximum retention pressures of 39 kPa and 9 kPa for water and FC-40. The mechanism for retention of non-polar liquids relies only on geometrical features and is, therefore, independent of the intrinsic properties (i.e., surface energy) of a membrane material. This study opens up the possibility of developing membrane structures for applications that require stable liquid-vapor interfaces in multi-phase systems. Future investigation into the role of surface defects and dynamic effects (e.g., high flow condition or evaporation) should be pursued to optimize the liquid retention performance and gain better understanding of the liquid pinning mechanism at sharp edges under non-equilibrium and non-ideal conditions.

Appendix A. Supplementary material

Supplementary data associated with this article can be found, in the online version, at https://doi.org/10.1016/j.jcis.2017.12.011.

References

[1] X. Yao, J. Gao, Y. Song, L. Jiang, Superoleophobic surfaces with controllable oil adhesion and their application in oil transportation, Adv. Funct. Mater. 21 (2011) 4270–4276.
[2] Z. Xue, S. Wang, L. Lin, L. Chen, M. Liu, L. Feng, L. Jiang, A novel superhydrophilic and underwater superoleophobic hydrogel-coated mesh for oil/water separation, Adv. Mater. 23 (2011) 4270–4273.
[3] R.W. Field, Surface science: separation by reconfiguration, Nature 489 (2012) 41–42.
[4] E. Gogolides, K. Ellinas, A. Tserepi, Hierarchical micro and nano structured, hydrophilic, superhydrophobic and superoleophobic surfaces incorporated in microfluidics, microarrays and lab on chip microsystems, Microelectron. Eng. 132 (2015) 135–155.
[5] A. Sridhar, C.L. Ong, S. Paredes, B. Michel, P. Brunschwiler, P. Parida, E. Colgan, T. Chainer, C. Gorle, K.E. Goodson, Thermal design of a hierarchical radially expanding cavity for two-phase cooling of integrated circuits, ASME 2015 International Technical Conference and Exhibition on Packaging and Integration of Electronic and Photonic Microsystems collocated with the ASME 2015 13th International Conference on Nanochannels, Microchannels, and Minichannels, American Society of Mechanical Engineers, 2015. V001T009A039-V001T009A039.
[6] C.J.M. Lasance, Advances In High-Performance Cooling For Electronics in, 2005.
[7] R. Mandel, A. Shooshtari, M. Ohadi, Thin-film evaporation on microgrooved heatsinks, Numer. Heat Transfer, Part A: Appl. (2017) 1–17.
[8] R. Ranjan, J.Y. Murthy, S.V. Garimella, A microscale model for thin-film evaporation in capillary wick structures, Int. J. Heat Mass Transf. 54 (2011) 169–179.
[9] J.W. Palko, L. Hyoungsoon, D.D. Agonafer, C. Zhang, J. Ki Wook, J. Moss, J.D. Wilbur, T.J. Dusseault, M.T. Barako, F. Houshmand, G. Rong, T. Maitra, C. Gorle, Y. Won, D. Rockosi, I. Mykyta, D. Resler, D. Altman, M. Asheghi, J.G. Santiago, K.E. Goodson, High heat flux two-phase cooling of electronics with integrated diamond/porous copper heat sinks and microfluidic coolant supply, in: 2016 15th IEEE Intersociety Conference on Thermal and Thermomechanical Phenomena in Electronic Systems (ITherm), 2016, pp. 1511–1517.
[10] J.L. LaSalle, Data Center Outlook, in, July 2016.
[11] Y. Sverdlik, Here's How Much Energy All US Data Centers Consume, 2016.
[12] A. Bar-Cohen, Gen-3 thermal management technology: role of microchannels and nanostructures in an embedded cooling paradigm, J. Nanotechnol. Eng. Med. 4 (2013) 020907.
[13] P.R. Parida, Reduced order modeling for chip-embedded micro-channel flow boiling, ASME 2015 International Technical Conference and Exhibition on Packaging and Integration of Electronic and Photonic Microsystems collocated with the ASME 2015 13th International Conference on Nanochannels, Microchannels, and Minichannels, American Society of Mechanical Engineers, 2015. V001T009A085-V001T009A085..
[14] S. Narayanan, A.G. Fedorov, Y.K. Joshi, Experimental characterization of a micro-scale thin film evaporative cooling device, in: Thermal and Thermomechanical Phenomena in Electronic Systems (ITherm), 2010 12th IEEE Intersociety Conference on, IEEE, 2010, pp. 1–10.
[15] M.P. David, J. Miler, J.E. Steinbrenner, Y. Yang, M. Touzelbaev, K.E. Goodson, Hydraulic and thermal characteristics of a vapor venting two-phase microchannel heat exchanger, Int. J. Heat Mass Transf. 54 (2011) 5504–5516.
[16] M.P. David, J.E. Steinbrenner, J. Miler, K.E. Goodson, Adiabatic and diabatic two-phase venting flow in a microchannel, Int. J. Multiph. Flow 37 (2011) 1135–1146.
[17] J. Palko, C. Zhang, J. Wilbur, T. Dusseault, M. Asheghi, K. Goodson, J. Santiago, Approaching the limits of two-phase boiling heat transfer: High heat flux and low superheat, Appl. Phys. Lett. 107 (2015) 253903.
[18] A. Tuteja, W. Choi, M. Ma, J.M. Mabry, S.A. Mazzella, G.C. Rutledge, G.H. McKinley, R.E. Cohen, Designing superoleophobic surfaces, Science 318 (2007) 1618–1622.
[19] A. Tuteja, W. Choi, J.M. Mabry, G.H. McKinley, R.E. Cohen, Robust omniphobic surfaces, Proc. Natl. Acad. Sci. 105 (2008) 18200–18205.
[20] T.L. Liu, C.-J.C. Kim, Turning a surface superrepellent even to completely wetting liquids, Science 346 (2014) 1096–1100.
[21] R. Hensel, R. Helbig, S. Aland, H.-G. Braun, A. Voigt, C. Neinhuis, C. Werner, Wetting resistance at its topographical limit: the benefit of mushroom and serif T structures, Langmuir 29 (2013) 1100–1112.
[22] R. Helbig, J. Nickerl, C. Neinhuis, C. Werner, Smart skin patterns protect springtails, PLoS One 6 (2011) e25105.
[23] S. Pan, A.K. Kota, J.M. Mabry, A. Tuteja, Superomniphobic surfaces for effective chemical shielding, J. Am. Chem. Soc. 135 (2012) 578–581.
[24] K. Golovin, D.H. Lee, J.M. Mabry, A. Tuteja, Transparent, Flexible, Superomniphobic Surfaces with Ultra-Low Contact Angle Hysteresis, Angewandte Chemie Int. Ed. 52 (2013) 13007–13011.
[25] A. Ahuja, J.A. Taylor, V. Lifton, A. Sidorenko, T.R. Salamon, E.J. Lobaton, P. Kolodner, T.N. Krupenkin, Nanonails: a simple geometrical approach to electrically tunable superlyophobic surfaces, Langmuir 24 (2008) pp. 9–14.
[26] W. Choi, A. Tuteja, J.M. Mabry, R.E. Cohen, G.H. McKinley, A modified Cassie-Baxter relationship to explain contact angle hysteresis and anisotropy on non-wetting textured surfaces, J. Colloid Interface Sci. 339 (2009) 208–216.
[27] R. Dufour, M. Harnois, Y. Coffinier, V. Thomy, R. Boukherroub, V. Senez, Engineering sticky superomniphobic surfaces on transparent and flexible PDMS substrate, Langmuir 26 (2010) 17242–17247.
[28] D.D. Agonafer, K. Lopez, J.W. Palko, Y. Won, J.G. Santiago, K.E. Goodson, Burst behavior at a capillary tip: Effect of low and high surface tension, J. Colloid Interface Sci. 455 (2015) 1–5.
[29] A. Glière, C. Delattre, Modeling and fabrication of capillary stop valves for planar microfluidic systems, Sens. Actuat., A 130 (2006) 601–608.
[30] H. Cho, H.-Y. Kim, J.Y. Kang, T.S. Kim, How the capillary burst microvalve works, J. Colloid Interface Sci. 306 (2007) 379–385.
[31] M.G. Hospital, Capillary Flow (2005) 192–197.
[32] P. Man, C. Mastrangelo, M. Burns, D. Burke, Microfabricated capillarity-driven stop valve and sample injector, in: Micro Electro Mechanical Systems, 1998. MEMS 98. Proceedings., The Eleventh Annual International Workshop on, IEEE, 1998, pp. 45–50.
[33] J.M. Chen, P.-C. Huang, M.-G. Lin, Analysis and experiment of capillary valves for microfluidics on a rotating disk, Microfluid. Nanofluid. 4 (2008) 427–437.
[34] T.-S. Leu, P.-Y. Chang, Pressure barrier of capillary stop valves in micro sample separators, Sens. Actuators, A 115 (2004) 508–515.
[35] B. Zhao, J.S. Moore, D.J. Beebe, Principles of surface-directed liquid flow in microfluidic channels, Anal. Chem. 74 (2002) 4259–4268.
[36] J.W. Suk, J.-H. Cho, Capillary flow control using hydrophobic patterns, J. Micromech. Microeng. 17 (2007) N11.
[37] A. Fluent, Ansys fluent theory guide, ANSYS Inc., USA 15317 (2011) pp. 724–746.
[38] K.A. Brakke, The surface evolver, Exp. Math. 1 (1992) 141–165.
[39] D. Attinger, C. Frankiewicz, A.R. Betz, T.M. Schutzius, R. Ganguly, A. Das, C.-J. Kim, C.M. Megaridis, Surface engineering for phase change heat transfer: A review, MRS Energy Sustain. 1 (2014) E4.
[40] J.W. Gibbs, The Scientific Papers of JW Gibbs, vol. 1, Dover, New York, 1961.
[41] G. Fang, A. Amirfazli, Understanding the edge effect in wetting: a thermodynamic approach, Langmuir 28 (2012) 9421–9430.
[42] H. Mayama, Y. Nonomura, Theoretical consideration of wetting on a cylindrical pillar defect: pinning energy and penetrating phenomena, Langmuir 27 (2011) 3550–3560.
[43] J. Brackbill, D.B. Kothe, C. Zemach, A continuum method for modeling surface tension, J. Comput. Phys. 100 (1992) 335–354.
[44] D.L. Youngs, Time-dependent multi-material flow with large fluid distortion, Numer. Methods Fluid Dyn. 24 (1982) 273–285.
[45] A. Fluent, 12.0 User's Guide, Ansys Inc, 2009.
[46] B. Lafaurie, C. Nardone, R. Scardovelli, S. Zaleski, G. Zanetti, Modelling Merging and Fragmentation in Multiphase Flows with SURFER, J. Comput. Phys. 113 (1994) 134–147.
[47] H. Lamb, Hydrodynamics, Cambridge University Press, 1932.
[48] S.M. Kang, S.M. Kim, H.N. Kim, M.K. Kwak, D.H. Tahk, K.Y. Suh, Robust superomniphobic surfaces with mushroom-like micropillar arrays, Soft Matter 8 (2012) 8563–8568.
[49] X. Zhu, Z. Zhang, X. Xu, X. Men, J. Yang, X. Zhou, Q. Xue, Facile fabrication of a superamphiphobic surface on the copper substrate, J. Colloid Interface Sci. 367 (2012) 443–449.
[50] E. Celia, T. Darmanin, E. Taffin de Givenchy, S. Amigoni, F. Guittard, Recent advances in designing superhydrophobic surfaces, J. Colloid Interface Sci. 402 (2013) 1–18.
[51] J. Berthier, F. Loe-Mie, V.-M. Tran, S. Schoumacker, F. Mittler, G. Marchand, N. Sarrut, On the pinning of interfaces on micropillar edges, J. Colloid Interface Sci. 338 (2009) 296–303.